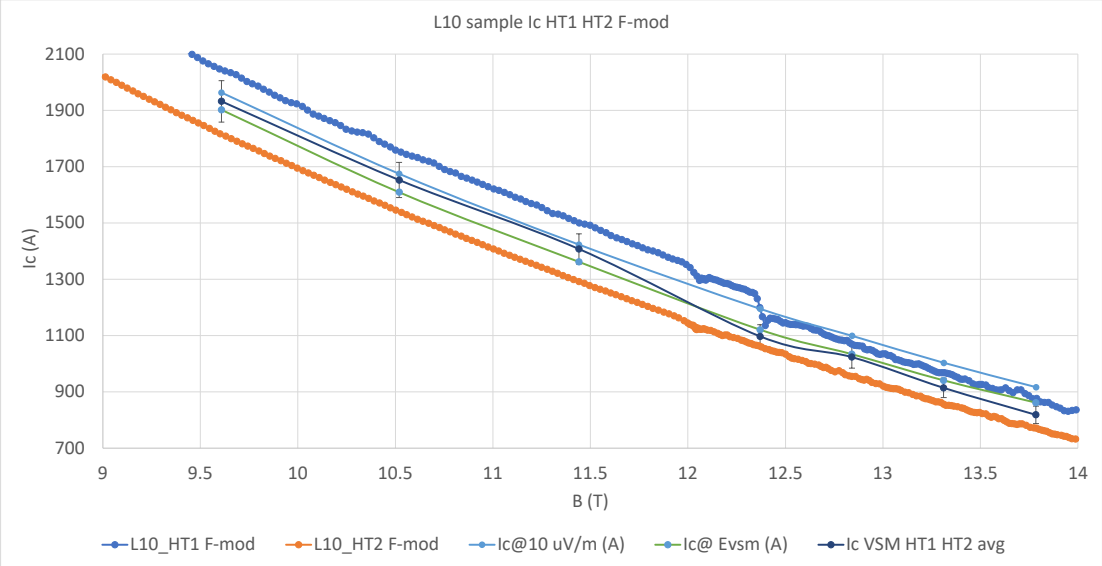

(a) *10% rolled samples numerical shape factor*

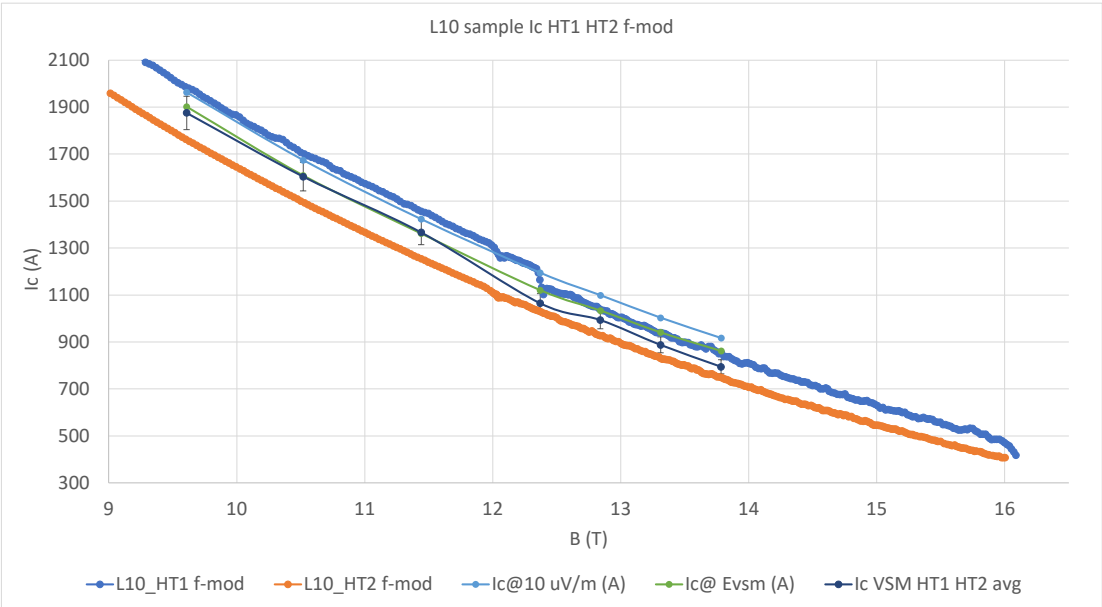

(b) *10% rolled samples analytical shape factor*

Figure 3.25: The plots show the interpretation of the m_{irr} signal by the the numerical and the analytical methods for L10 samples.

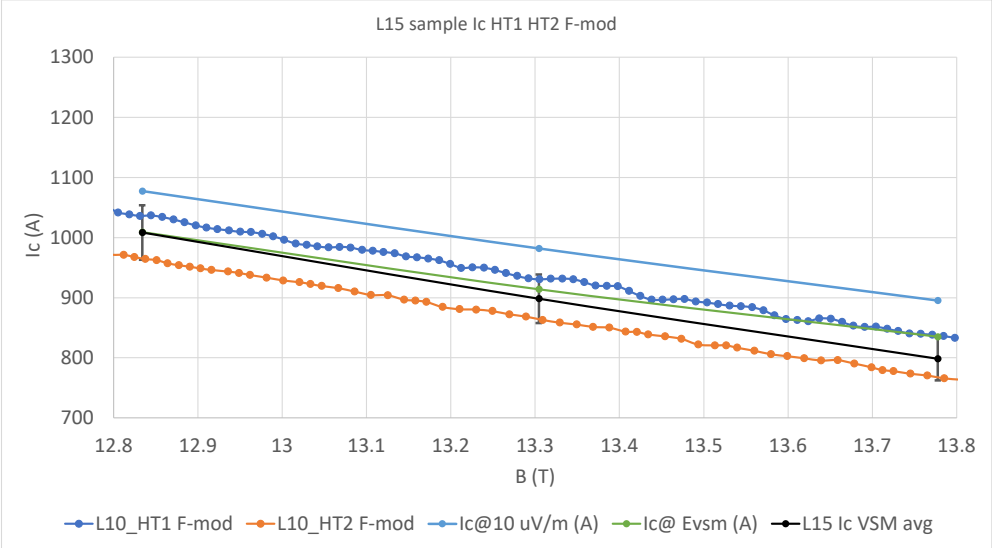

(a) *15% rolled samples numerical shape factor*

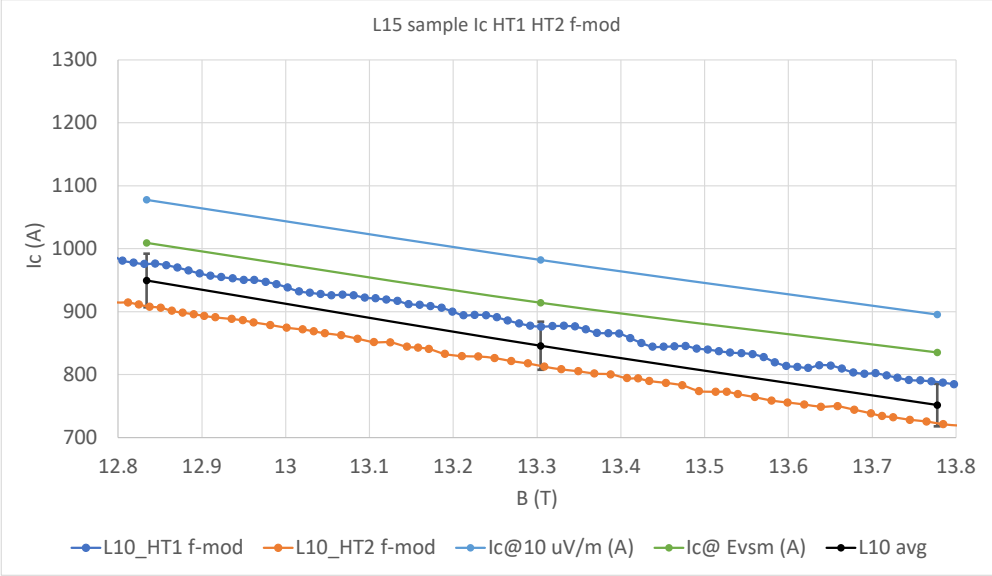

(b) *15% rolled samples analytical shape factor*

Figure 3.26: The plots show the interpretation of the m_{irr} signal by the the numerical and the analytical methods for L15 samples.

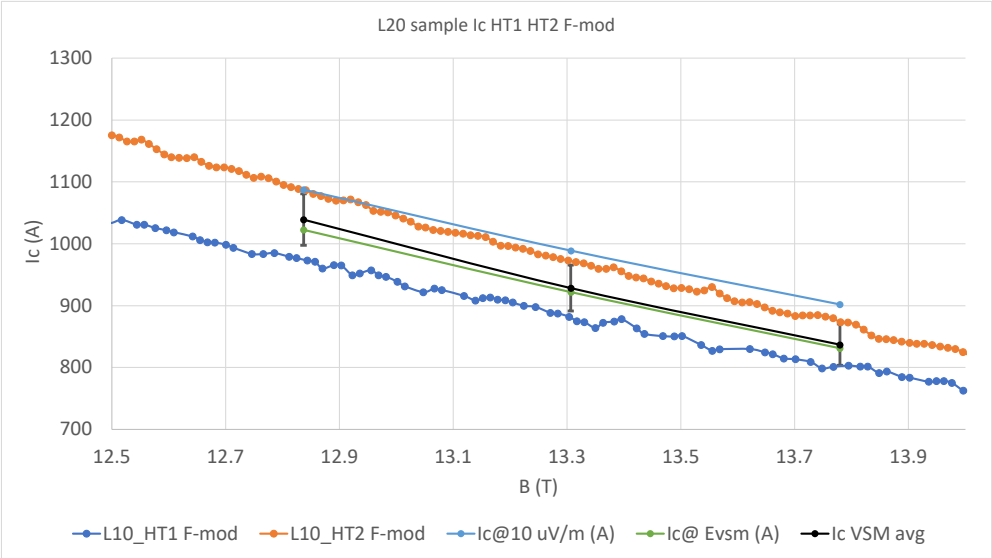

(a) *20% rolled samples numerical shape factor*

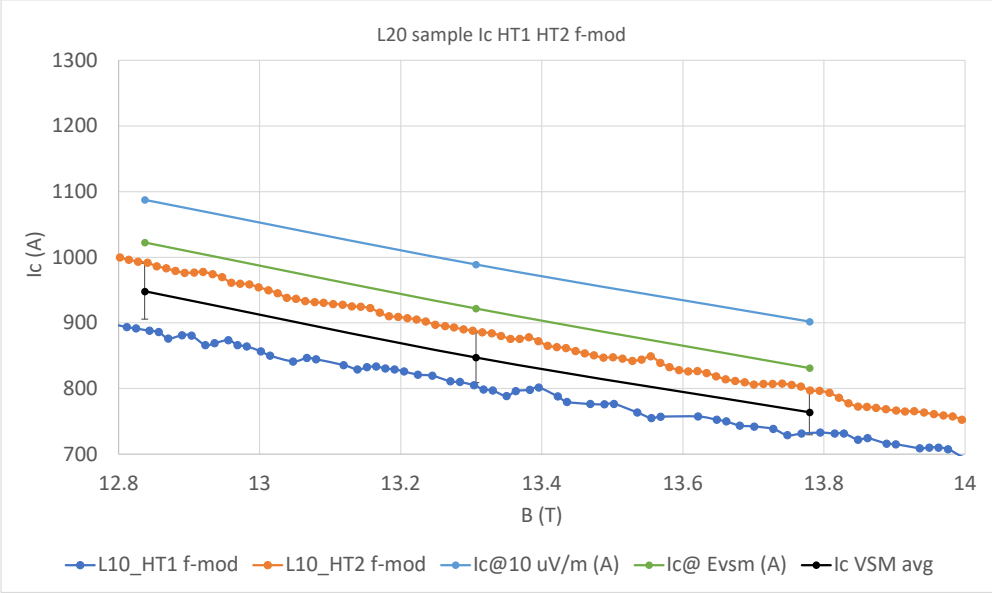

(b) *20% rolled samples analytical shape factor*

Figure 3.27: The plots show the interpretation of the m_{irr} signal by the the numerical and the analytical methods for L20 samples.

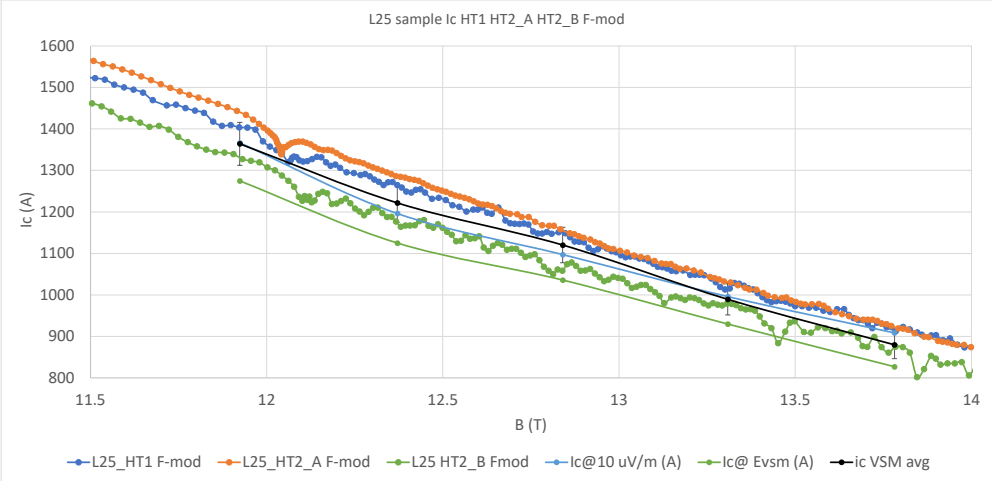

(a) *25% rolled samples numerical shape factor*

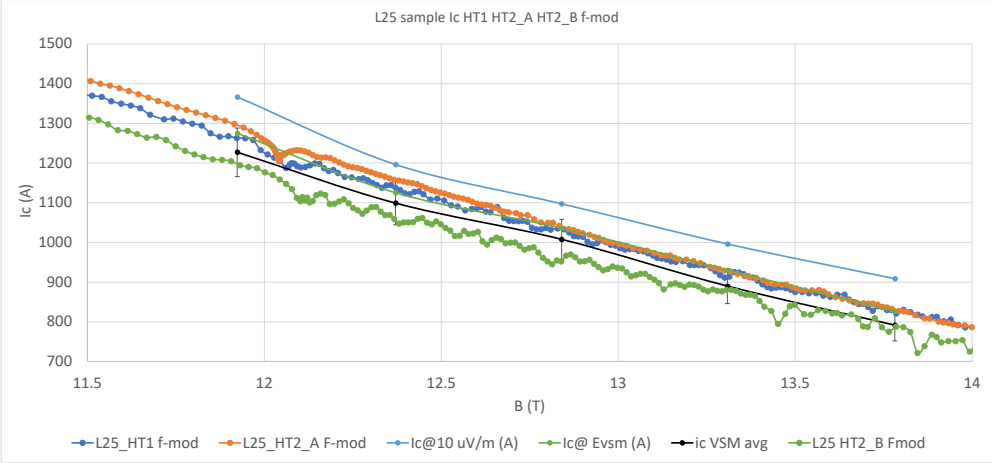

(b) *25% rolled samples analytical shape factor*

Figure 3.28: The plots show the interpretation of the m_{irr} signal by the the numerical and the analytical methods for L25 samples.

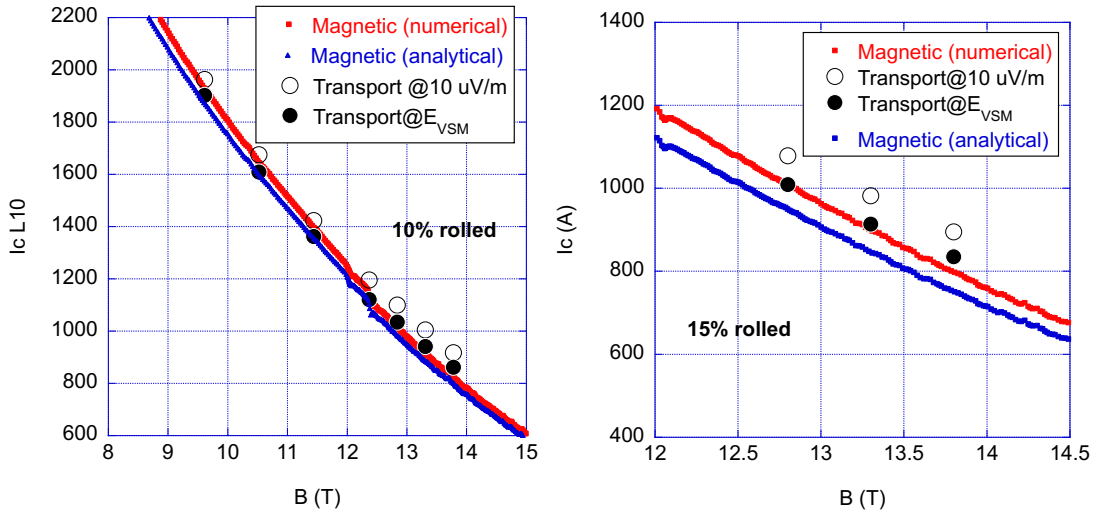

(a) *10% rolled samples* (b) *15% rolled samples*

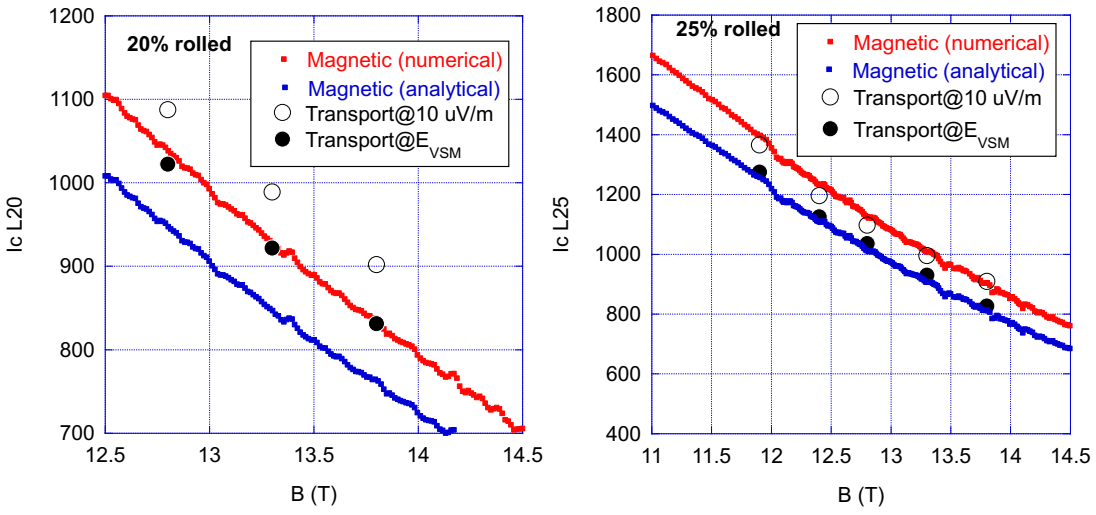

(c) *20% rolled samples* (d) *25% rolled samples*

Figure 3.29: The plots summarize the results of the numerical (red) and analytical (blue) models used to extract I_c from the VSM data, compared to the critical current from the VAMAS measurements (empty dots are not scaled, i.e., $E_c = 10, \mu V/m$; black dots are scaled to E_{VSM}).

A global overview of the correlation between magnetic and transport critical current is presented in the plot of Figure 3.30. It shows that all the VSM data, with the exception of L25, agree within 5% with their respective VAMAS counterparts.

Another way to look at same result is represented by the VSM normalized critical current plots, fig. 3.31. We can claim no critical current degradation, in agreement with the VAMAS normalized I_c (fig. 3.10b), only if we use the numerical shape factor to extract I_c from the m_{irr} signal. Instead, the analytical shape factor leads to an apparent critical current degradation which, in our opinion, is a manifestation of the circular approximation. Anyway also the numerical model can fail, as we can see in the L25 case. Herein, paradoxically, we see an improvement of the critical current, almost the 15% more at 10.5 T. In the next section we'll analyze this aspect in a more quantitative way.

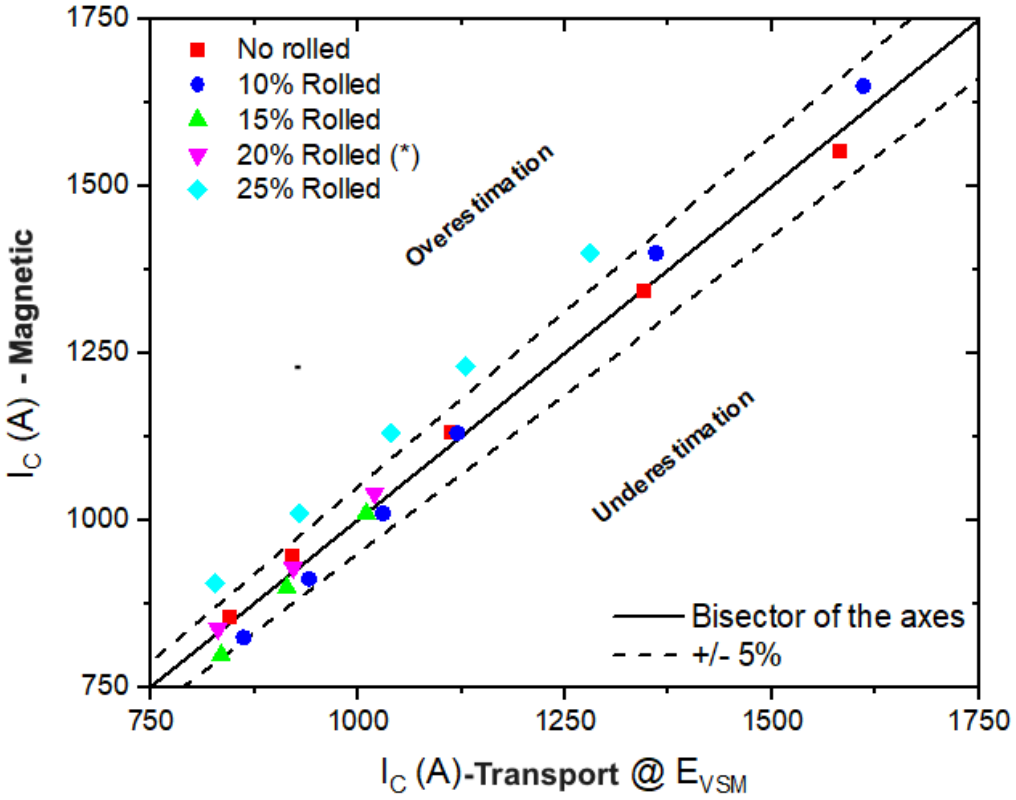

Figure 3.30: Correlation plot between magnetic (numerical shape factor analysis) and transport critical current. The dashed lines delimit the ± 5% error region calculated with errors propagation.

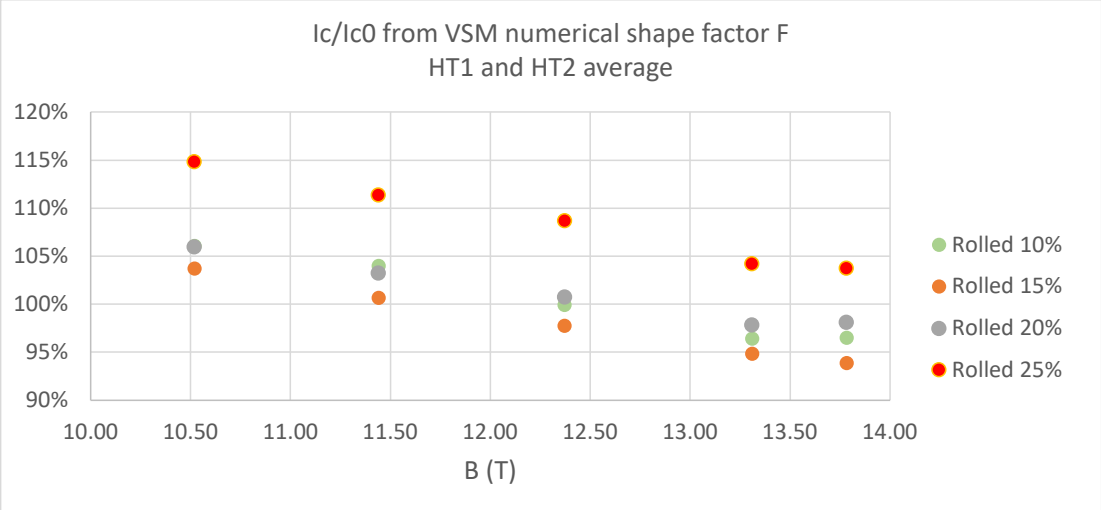

(a) *The normalized VSM critical current in the case of numerical shape factor elaboration.*

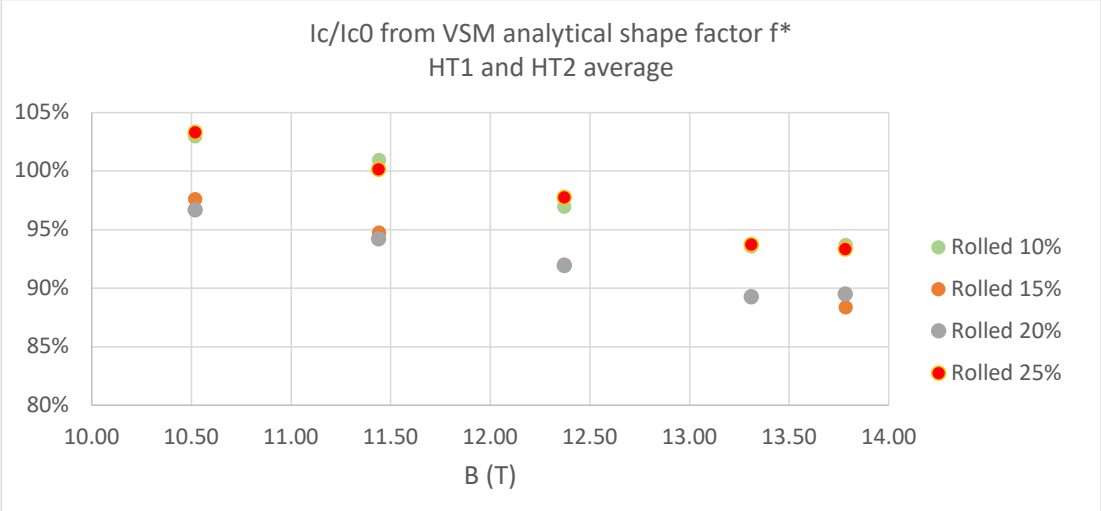

(b) *The normalized VSM critical current in the case of analytical shape factor elaboration.*

Figure 3.31: The normalized critical current plot for numerical and analytical shape factor.

We conclude this section reporting the analysis of the $B_{c2}(4.2\,K)$ values for the rolled samples, either for the numerical and analytical model. The B_{c2} field can be obtained by the fitting the J_c curve with eq. 3.2. We remember that B_{c2} is also a function of the strain state, through the strain function. Therefor, it's behaviour is a symptom of the residual strain in the wire after lamination. The B_{c2} value at $4.2\,K$ is expected to be, thanks to eq. 3.3, around $25.5\,T$ for the virgin wire. Concerning the C parameter in eq. 3.2, we can say that it's related to the intensity of the signal. We report the fitting equation for clarity

$$J_c^L(B, 4.2\,K) = \frac{C}{B}\left(\frac{B}{B_{c2}}\right)^{0.5}\left(1 - \frac{B}{B_{c2}}\right)^2 \tag{3.26}$$

The J_c data are obtained from the critical current plot showed in fig. 3.24 and fig. 3.29 simply dividing by the correspondent S_{SC} values listed in tab. 3.7. The fit is done with the Kaleidagraph software with the free parameter B_{c2} and C. The results are visible in table 3.8.

Lamination	**Numerical model**		**Analytical model**	
	C (10^5 ATm^{-2})	**Bc2** (T)	**C** (10^5 ATm^{-2})	**Bc2** (T)
0	2.364	25.71	2.378	25.71
10	2.477	24.26	2.400	24.28
15	2.530	24.43	2.379	24.44
20	2.795	24.21	2.546	24.23
25	3.041	24.12	2.732	24.14

Table 3.8: Comparison between Numerical and Analytical models for the fitting parameter of J_c from VSM data. In the Lamination columns 0 means no lamination at all, i.e. the virgin sample.

We can see a similar trend in the values of B_{c2} for both models, fig. 3.32a. There is an initial strong decrease due to the first laminating process at 10% and then a flattening around 24 T. This indicates that the effects of residual stress are significant up to a certain level of lamination. Considering that heat treatment also contributes to the release of residual stress in the copper matrix, we can conclude that the effects of pre-HT deformation on B_{c2}, through the strain function, are negligible for laminations between 10% and 25%.

Regarding the parameter C, the two models show a discrepancy, fig. 3.32b. Only the numerical model, through the shape factor, captures a strong increasing

trend in signal intensity. This underlies the good agreement between the transport I_c values and the corresponding critical currents obtained from the VSM with the numerical shape factor. Additionally, the value of C at 25% lamination supports the interpretation of an overestimation of the m_{irr} signals due to inter-bundle currents among fused bundles.

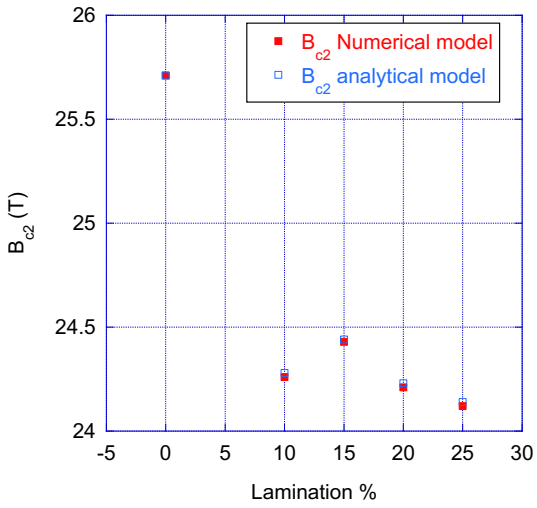

(a) $B_{c2}(4.2\,K)$ *as parametric fit of* J_c *from VSM data.*

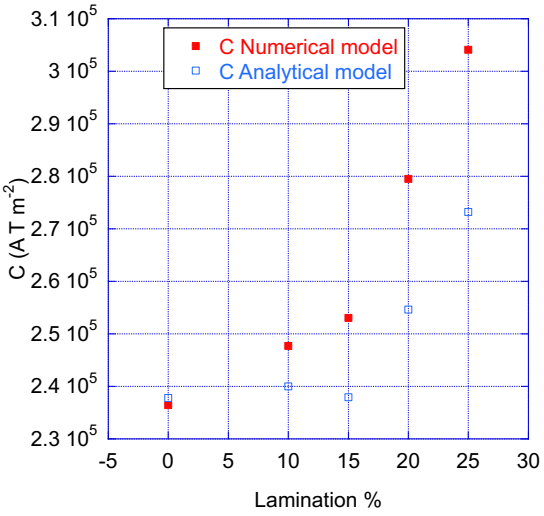

(b) $C(4.2\,k)$ *as parametric fit of* J_c *from VSM data.*

Figure 3.32: The plots show the data of table 3.8 versus the lamination percentage.

3.9 Comparison between VAMAS and VSM data

The self-field corrections and the scaling procedure of the VAMAS data are necessary steps to compare transport and magnetization critical currents. Nevertheless we need a quantitative way to measure their compatibility. At this purpose we assume $I_c^{VAMAS;L}$, hereafter referred to more briefly as I_c^L, as best estimator and suppose the VSM $I_c^{VSM;L}$ to be a Gaussian observable centred in I_c^L, with standard deviation $\delta I_c^{VSM;L}$ estimated by the propagation errors applied to eq. 3.24

$$\frac{\delta I_c^{VSM;L}}{I_c^{VSM;L}} = \sqrt{\left(\frac{\delta m_{irr}}{m_{irr}}\right)^2 + \left(\frac{\delta l}{l}\right)^2 + \left(\frac{\delta F}{F} + \frac{\delta S_{SC}}{SC}\right)^2} \tag{3.27}$$

The relative error in m_{irr} is about 1%; $\delta l/l$ is variable from 0.1% to 2%; $\delta F/F$ and $\delta S_{SC}/S_{SC}$ cannot be considered independent quantity since are derived from the same SEM image analysis. The relative error in $I_c^{VSM;L}$ results in the range from 3 to 5%.

Our statistical approach is based on the parameter t, measuring the discrepancy respect to the standard deviation at a single B field value

$$t_L(B) = \frac{|I_c^{VSM;L}(B) - I_c^L(B)|}{\delta I_c^{VSM;L}(B)} \tag{3.28}$$

Since VAMAS measurements correspond to a set of points $(B_i, I_c^L(B_i))$, to summarize how the compatibility between $I_c^{VSM;L}$ and I_c^L is spread out over the B values, i.e. for a given L value, we look at average of t and its standard deviation. So we define

$$\bar{t}_L = 1/N \sum_i^N \frac{|I_c^{VSM;L}(B_i) - I_c^L(B_i)|}{\delta I_c^{VSM;L}(B_i)} \tag{3.29}$$

From a global perspective, by defining $\bar{t}_L$, we aim to summarize the statistical compatibility of the data obtained at different external field values B. By selecting a mean compatibility criterion within $2\delta I_c^{VSM;L}$, the following conditions must be satisfied

$$\bar{t}_L \leq 1.0 \quad and \quad \sigma_{t_L} \leq 1.0 \tag{3.30}$$

We look also at the mean relative difference, i.e. the average along the B_i field values of the quantity

$$rel.diff_L(B_i) = \frac{|I_c^{VSM;L}(B_i) - I_c^L(B_i)|}{I_c^L(B_i)} \tag{3.31}$$

We can use the previous definition to compare the analysis based on the numerical or analytical shape factors. We have to underling that this comparison is meaningful only if eq. 3.29 is calculated respect to the scaled VAMAS data, also for the analytical model. The result is in table 3.9. According to the criterion indicated by eq. 3.30 the two methods agree with the transport measurements until the 10% of rolling. In the case of L15 and L20, the analytical model is incompatible with the transport measurements. This means that, unlike the numerical model, the analytical one is unable to capture the differences due to the deformation of the bundles and their orientation with respect to the external magnetic field. At 25% of lamination, there is an inversion such that the analytical model becomes highly compatible with the transport measurements, while the numerical model exceeds the 2σ on average. In our opinion, this paradox is a manifestation of the bundles merging which leads to lose the non-coupling current hypothesis over the 20% of rolling. This results in a stronger m_{irr} signal, as observed also in [51]. In the case of the analytical model, the more intense signal is offset by the shape factor, which remains more or less constant, see tab. 3.7. This causes the apparent compatibility with the transport measurements scaled to the criterion E_c^{VSM}. On the contrary, the interpretation made by the numerical model leads to an improved critical current, which is just an artifact, an indication of a threshold, above the 20% of rolling, that we can't exceed, otherwise our method cannot be applied.

Rolling %	Numerical model			Analytical model		
	$\bar{t}_L$	σ_{t_L}	$< rel.diff_L >$	$\bar{t}_L$	σ_{t_L}	$< rel.diff_L >$
0	0.6	0.4	0.6%	0.7	0.4	1.3%
10	0.7	0.4	-0.5%	1.0	0.8	-3.4%
15	0.5	0.5	-2.1%	1.9	0.5	-7.8%
20	0.4	0.3	1.6%	1.7	0.3	-7.3%
25	2.1	0.3	7.3%	0.9	0.2	-3.5%

Table 3.9: The table provides a comprehensive overview of the compatibility between the VSM critical currents and the VAMAS ones.

Chapter 4

ASTRACT Part II

The second part of the ASTRACT project is devoted to design, testing and commissioning a sample-holder (SH) to perform critical current characterization of Nb_3Sn wires at 4.2 K, in a range from 10 to 13 T, in a controlled transverse strain condition. We should remark that the word "strain" is a little bit abused. As noted in the ASTRACT part I, we can't measure directly the internal strain state of the wire. And also the diameter deformation as defined by eq. 3.1 is not easy to be measured in a real-time critical current measurement. The only way is looking for a correlation between a physical observable, for example the distance between two flanges, and the diameter contraction of the wire. For instance, the final goal is finding a correlation with respect to the invariants of the internal strain field defined by eq. 2.25. This kind of correlations can be achieved only through FEM simulations. At the moment is too early to deeply go inside this subject. Thus, this chapter will be mainly dedicated to describe the steps leading to the experimental setup. ASTRACT part II is still a work in progress, which required an extension of the project until to the end of 2024. The design phase has been concluded, as well as the material procurement and the manufacturing of all main components in our workshop. Nowadays, we are assembling the SH, evaluating solutions to problem which could not be expected during the design phase. In this chapter we'll describe the sample-holder design, the choices behind it, and we'll try to get in touch with the assembling and testing issues.

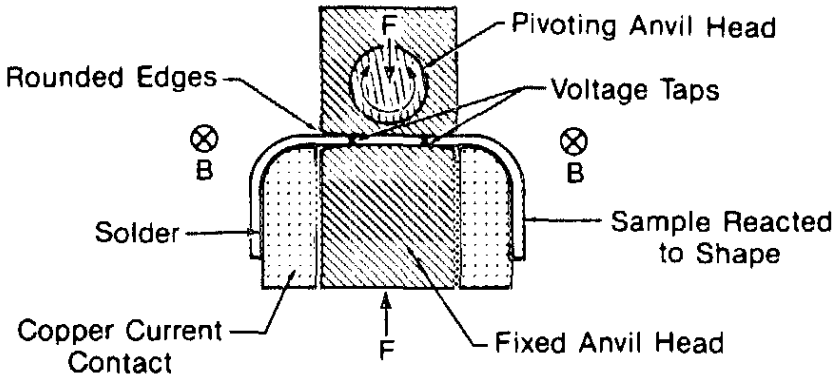

Figure 4.1: A schematic view of the stress test apparatus developed by Ekin in the 1987

4.1 A brief look in the past

We have seen in section 2.3.4 the WALTER spring modified by the Senatore's group in Geneve University. Before it, the pioneristic study about the effect of transverse stress on Nb_3Sn wires is represented by the Ekin's work on the subject [21]. In fig. 4.1 we can see the experimental setup chosen by him.

Essentially Ekin developed a U-shape setup where the anvil exerts a uniform stress on the sample along fews centimeters. We note that the critical current is characterized versus the applied stress, not transverse strain.

Another example of a comprehensive study about this subjects is the Luisa Chiesa's PhD Thesis [17]. In that work different sample-holder are manufactured to study the effects of transverse stress affecting superconducting cables or wires. A very interesting geometry showed in the Chiesa's work is the hairpin model. It's a U-shape geometry where forces are applied on the long lateral straight part of the sample, in a background field generated by a split-coil magnet, fig.4.2. This configuration is particularly interesting because it was used to measure a single Nb_3Sn strand, not only to characterize I_c versus the transverse stress, but also to evaluate its mechanical properties like the transverse Young's modulus. Thus, this means that the Author was able to measure the transverse displacement of the test sample against the applied force per unit length. To our purpose it's important to recall more details about this experiment, so we deserve a section to describe its geometry and results.

The split magnet system creates a magnetic field perpendicular to the vertical direction and gives the flexibility to use a hairpin sample with legs that connect to the current leads without having to bend the sample out of its plane (Fig. 4.5). The field and current direction create a natural load in the same direction as the mechanically applied load applied.

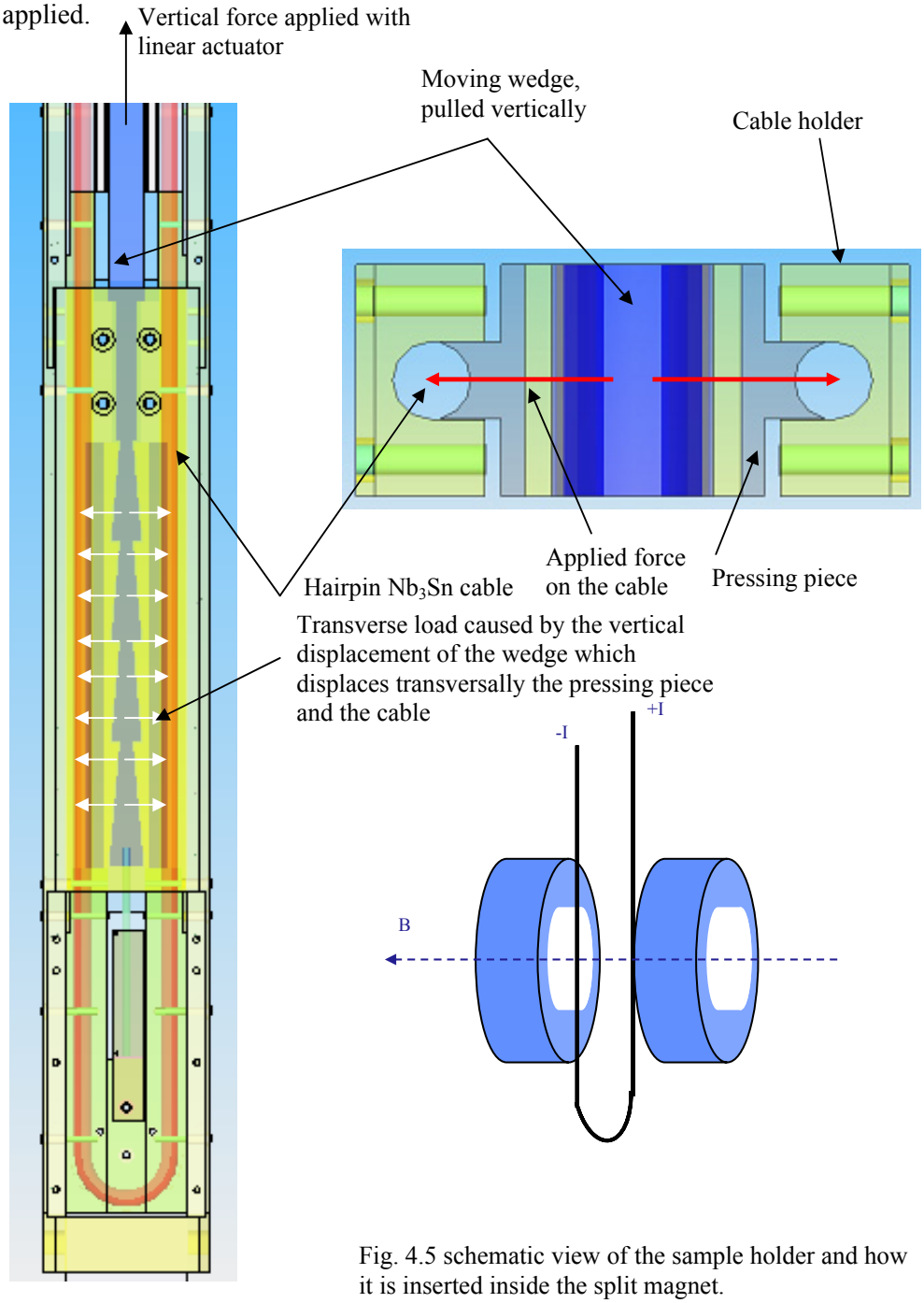

Fig. 4.5 schematic view of the sample holder and how it is inserted inside the split magnet.

Figure 4.2: The scheme shows the hairpin sample holder structure and the generation of the applied load on samples. The text upside the picture is a quote from the Author's thesis and is referencing to fig. 4.5, the split coil representation.

4.1.1 The hairpin setup at NHMFL in 2007

In this configuration the applied load is generated by the vertical movement of segmented wedges. Next to them there are two matching pieces that are constrained vertically and can only slide horizontally. They touch two pressing pieces underneath which the sample is located, thus the sample is pressed in between the holder and the pressing piece. The vertical force is created by a linear actuator outside the dewar. The force is measured by a load cell close to the actuator. We do not enter in the details about the conversion of the vertical force into the acting force on the sample, essentially they are based on analytical considerations about the force distribution. The sample holder is made by TiAlV to match as much as possible the Nb_3Sn thermal contraction. The instrumentation is made with voltage taps, temperature sensors, Hall probes and strain-gauges to monitor the vertical displacement of the wedges. From the vertical displacement raw data, with some geometrical consideration, (see Chapter 3 and 4 in [17]), it's possible to achieve the horizontal displacement and the transverse Young's modulus of the wire. With this setup they could measure cables but also a single strand, which is the most interesting case for us. The single strand was an Oxford, Nb_3Sn Internal Tin, with a diameter of 0.82 mm and Jc at 12 T and 4.2 K of around 1014 A/mm^2. Pulling up the wedges with a vertical force up to 1500 N they could exert up to 8600 N of horizontal force over the 150 mm of sample length. The mechanical system was acting as force multiplier. So, the first result in terms of critical current degradation is depicted in fig. 4.3a. The normalized critical current shows a sign of degradation approaching an applied force of around 40 kN/m. In terms of transverse displacement, fig. 4.3b, this correspond to 70 μm on a diameter of 0.82 mm. The resulting transverse Young's module is reported in fig. 4.3c. We note that the plots correlate the y-axis to force per unit length, not to applied stress. As pointed out by the Author, the evaluation of the applied stress is generally based on the acting force over the effective surface

$$\sigma = \frac{F_{acting}}{D_{strand}\, l_{pressed}} \tag{4.1}$$

This is a rule of thumb leading to an underestimation of the real stress or, vice-versa, leading to an overestimation of the force you need to have a certain stress value. In the Chiesa's work the main tool to face this approximation is the an-

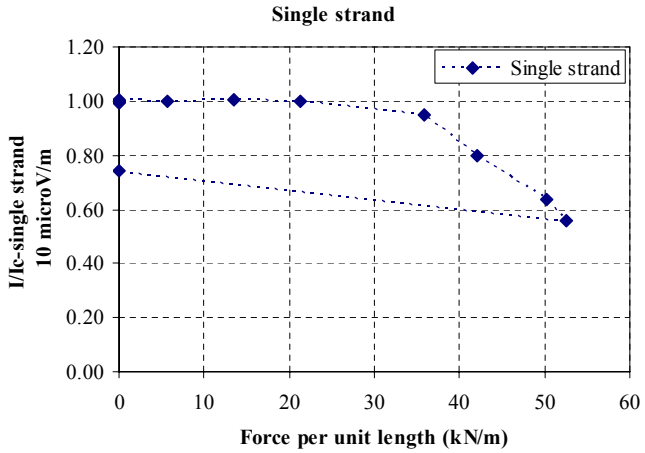

(a) Normalized critical current as a function of force per unit length for the single strand sample.

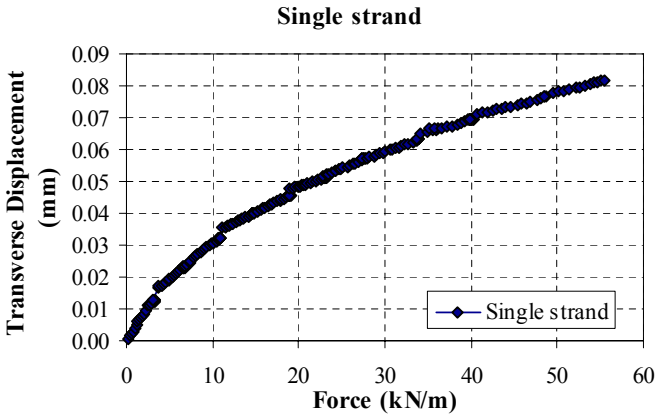

(b) Transverse displacement as a function of force per unit length for the single strand sample.

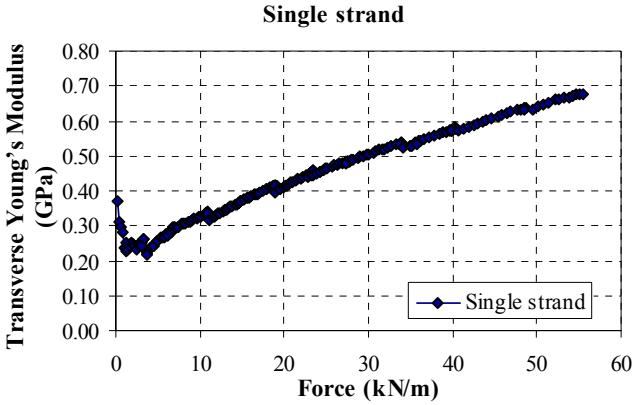

(c) Transverse Young's module as a function of force per unit length for the single strand sample.

Figure 4.3: Main results from [17] about the single strand measurements with the hairpin sample holder.

alytical approach through the Hertzian contact theory applied in three different conditions. We are interested just in one of them, the case about a cylinder pressed between two flat plates, so briefly we'll summarize its key points. Further details can be found in the Appendix III of [17].

4.1.2 Hertzian contact of a cylinder between two flat plates

The origin of contact mechanics is due to Hertz in 1892. To delve in more recent development of the subject, one could refer to Timoshenko in [30]. Let us start directly with the assumptions of the theory, which can be summarized in the following conditions about the contact characteristic:

1. it must be small compared to the dimensions of each body so that the local stress does not influence the general behavior of the solid
2. it must be small compared to the relative radii of curvature of the surfaces so that the strains in the contact region are sufficiently small to lie within the linear theory of elasticity.
3. the two surfaces are assumed to be frictionless

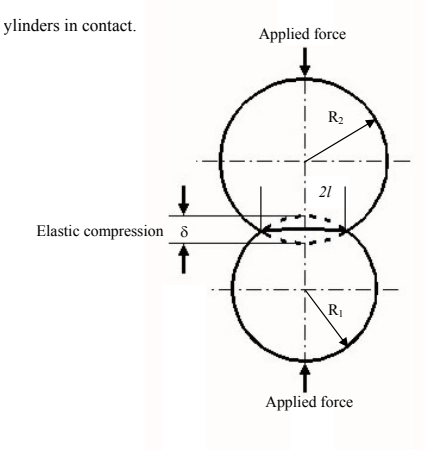

Figure 4.4: Schematic view of two long cylinders in contact.

Referring to fig. 4.4, if the significant dimension of the contact area is $2l$ and the relative radius of curvature R, the significant radii of each body R_1 and R_2 and their length and depth L, the assumptions made in the Hertz theory can be summarized as:

- the surfaces are continuous and non conforming: $2l << R$
- the strains are small: $2l << R$

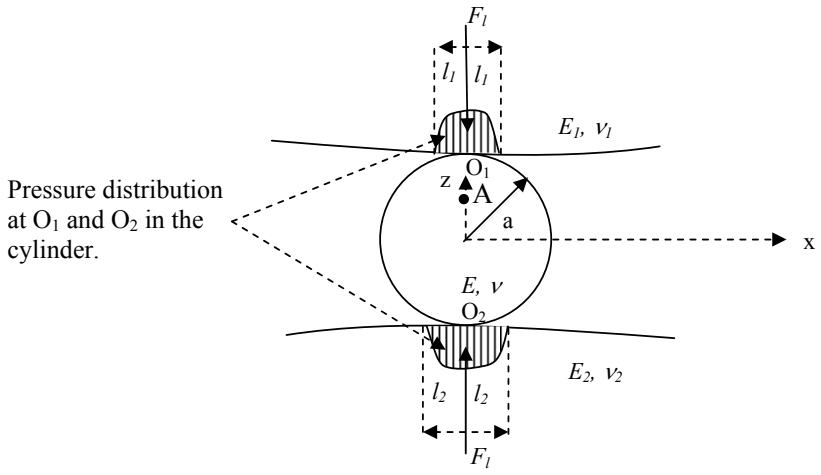

Figure 4.5: Cylinder in contact with two solids. The contact pressure distribution developed in the cylinder is shown in the figure and is used to estimate the contact width $2l_1$, $2l_2$.

- each solid can be considered as an elastic half space: $2l << R_{1,2}$, $2l << L$

- the surfaces are frictionless

The case of a cylinder of radius a between two plates can be represented as in fig. 4.5. We adapt the general formulas reported in [17] making the following assumptions: the plates are planar, $R_{1,2} \to \infty$, and made by the same material, $E_1 = E_2$; the cylinder and the plates have the same Poisson's coefficient, $\nu = \nu_1 = \nu_2$; E is the cylinder Young module and F is load applied per unit lenght. By this way we have the equation fitting our design which will be explained in the upcoming section. This tuning of the equations doesn't change the final result we are going to learn from the Chiesa's work. As depicted in fig. 4.5 the core of the Hertzian theory is the pressure contact profile acting on the points O_1 and O_2. The basic assumption is that this pressure has a parabolic profile. The consequences are the following:

- Given a compressive load per unit length F (kN/m) the semi-contact width l is

$$l^2 = \frac{4Fa}{\pi}(1-\nu^2)\frac{E_1 + E}{E_1 E} \tag{4.2}$$

- The total displacement of the cylinder diameter along the vertical axis is

$$\delta = 2F\frac{(1-\nu^2)}{\pi E}\left(2ln\left(\frac{4a}{l}\right)-1\right) \tag{4.3}$$

- The stress acting in points O_1 and O_2 is

$$\sigma = \frac{F}{2l} \tag{4.4}$$

Thanks to the Hertzian contact theory the Author in [17] was able to achieve a more realistic relation between I_c and the applied stress, see fig. 4.6, with respect to the standard choice to evaluate the stress as force divided by the effective surface (Nominal pressure). In the plot there are curves concerning three different possibilities in the contact topology, nevertheless we can see that the irreversible stress is approaching values close to 200 MPa. This is an important result that will be discovered again, for example in [60], more years later.

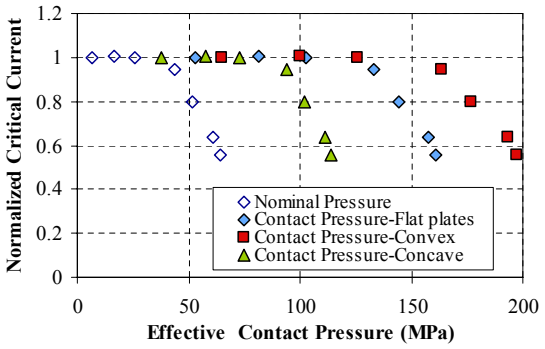

(a) Single strand results: nominal pressure and effective contact pressure for different contact types.

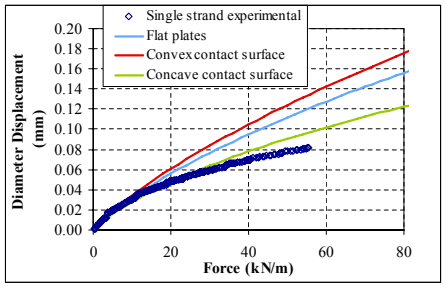

(b) Displacement of a single strand, 0.82 mm in diameter. Comparison between measurements and numerical evaluations.

Figure 4.6: The main Chiesa's result for a single strand applying the Hertzian contact equations. The parameter used are: $E = 0.95$ GPa strand Young's module; $E_1 = E_2 = 100$ GPa pressing plate Young's module; $\nu = 0.3$

In terms of diameter displacement, fig. 4.6b, the Hertzian theory show a good agreement with the experimental measurements at low load, where also the three type of contact converge on the same curve. At high load the agreement is lost, probably because the model is not able to account the non-elastic behaviour.

About this point we note that the transverse Young Module's of the strand is a fitting parameter. Quoting the Author:

> *In this analysis, Young's modulus of a strand for a transverse load was used as fitting parameter to analyze the experimental displacement data. For the single strand data, the Young's modulus value of E = 0.95 GPa was selected to obtain the best fit. On the other hand, the larger value of about E = 4 GPa gave better fitting for the displacement data of the 3-strand and the 45-strand samples. It is difficult to determine the absolute values of the transverse Young's modulus of a strand from the present experiments since the experiment itself was not designed to measure Young's modulus. Those measurements would require a dedicated experiment using an absolute method to determine the displacement-force curves. In the present experiment, the Young's modulus values come as extra measurements with little effort and offer insight on the mechanical behavior of the different samples.*

The transverse Young's modulus of a Nb_3Sn strand is a necessary input to apply the equations based on the Hertzian contact. In 2023, Vallone et al. suggested in [67] that elasto-plastic models may be more accurate in interpreting measurements of mechanical properties of Nb_3Sn cable stacks. In this regard, they propose an average value of the transverse Young's modulus for a Rutherford cable of approximately 26 GPa at 4.5 K (47 GPa at 300 K). Intuitively, we can imagine that the RRP Nb_3Sn wire has a transverse Young's modulus lower than the longitudinal one, given that the presence of voids in the cores may confer lower rigidity in the transverse direction. Vallone also showed in [68] how a transverse Young's modulus value of 20 GPa may better describe the observed mechanical behavior in MQXF short models. Furthermore, complicating the picture even further, the strands in the cable are twisted, so the geometry and heterogeneity of such system would lead one to question whether the same concept of Young's modulus is directly applicable. However, if we want to employ Hertzian contact theory to estimate the transverse deformation that we will impose, we need to delimit the possible values of the Young's modulus of the strand. For this purpose, in a conservative manner, the previous considerations can help us to consider values in the range between 1 and 40 GPa.

The Chiesa's work is very impressive. To our knowledge is the first study, and maybe the only one, attempting to measure the transverse displacement during a critical current measurement of a Nb_3Sn strand. However, there is not a direct correlation between this two data. In our opinion it deserved to be mentioned in the spirit of the ASTRACT project, even because it is a source of important data to use as reference values in the development of our sample-holder. From Chiesa's work, we can understand how to use the Hertzian contact formula to estimate the distance range we should measure in our setup. What is missing is the a priori knowledge of the wire's transverse Young's modulus. Therefore, a sensitivity analysis will be necessary.